

X-ray grating interferometer for biomedical imaging applications at Shanghai Synchrotron Radiation Facility

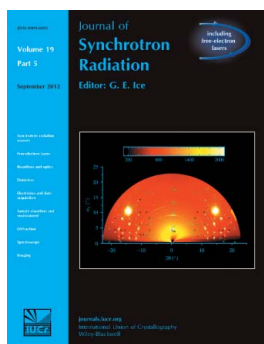
Yan Xi, Binqun Kou, Haohua Sun, Juncheng Qi, Jianqi Sun, Jürgen Mohr, Martin Börner, Jun Zhao, Lisa X. Xu, Tiqiao Xiao and Yujie Wang

J. Synchrotron Rad. (2012). **19**, 821–826

Copyright © International Union of Crystallography

Author(s) of this paper may load this reprint on their own web site or institutional repository provided that this cover page is retained. Reproduction of this article or its storage in electronic databases other than as specified above is not permitted without prior permission in writing from the IUCr.

For further information see <http://journals.iucr.org/services/authorrights.html>



Synchrotron radiation research is rapidly expanding with many new sources of radiation being created globally. Synchrotron radiation plays a leading role in pure science and in emerging technologies. The *Journal of Synchrotron Radiation* provides comprehensive coverage of the entire field of synchrotron radiation research including instrumentation, theory, computing and scientific applications in areas such as biology, nanoscience and materials science. Rapid publication ensures an up-to-date information resource for scientists and engineers in the field.

Crystallography Journals **Online** is available from journals.iucr.org

X-ray grating interferometer for biomedical imaging applications at Shanghai Synchrotron Radiation Facility

Yan Xi,^{b,c} Binqun Kou,^a Haohua Sun,^a Juncheng Qi,^d Jianqi Sun,^{b,c} Jürgen Mohr,^e Martin Börner,^e Jun Zhao,^{b,c*} Lisa X. Xu,^{b,c*} Tiqiao Xiao^{d*} and Yujie Wang^{a*}

^aDepartment of Physics, Shanghai Jiao Tong University, Shanghai 200240, People's Republic of China, ^bSchool of Biomedical Engineering, Shanghai Jiao Tong University, Shanghai 200240, People's Republic of China, ^cMed-X Research Institute, Shanghai Jiao Tong University, Shanghai 200040, People's Republic of China, ^dShanghai Institute of Applied Physics, Chinese Academy of Sciences, Shanghai 201800, People's Republic of China, and ^eKarlsruhe Institute of Technology, Institute for Microstructure Technology, Hermannvon-Helmholtz-Platz 1, 76344 Eggenstein-Leopoldshafen, Germany. E-mail: junzhao@sjtu.edu.cn, lisaxu@sjtu.edu.cn, tqxiao@sinap.ac.cn, yujiewang@sjtu.edu.cn

An X-ray grating interferometer was installed at the BL13W beamline of Shanghai Synchrotron Radiation Facility (SSRF) for biomedical imaging applications. Compared with imaging results from conventional absorption-based micro-computed tomography, this set-up has shown much better soft tissue imaging capability. In particular, using the set-up, the carotid artery and the carotid vein in a formalin-fixed mouse can be visualized *in situ* without contrast agents, paving the way for future applications in cancer angiography studies. The overall results have demonstrated the broad prospects of the existing set-up for biomedical imaging applications at SSRF.

© 2012 International Union of Crystallography
Printed in Singapore – all rights reserved

Keywords: X-ray grating interferometer; X-ray phase-contrast imaging; X-ray tomography; angiography.

1. Introduction

Conventional biomedical X-ray imaging techniques are based on the absorption capabilities of materials. When applied to image soft tissues, their effectiveness is rather limited because soft tissues absorb X-rays very weakly. Nonetheless, in many circumstances it is important to differentiate various soft tissues with high spatial resolution. For instance, the morphology of blood vessels during the tumour angiogenesis can provide valuable insights on the cancer growth mechanisms (Hanahan & Weinberg, 2000; Sekka *et al.*, 2000). To visualize these blood vessels an imaging technique which can distinguish tissues with very similar densities is needed. The traditional way to solve this problem is through the injection of contrast agents, but they may cause side effects in some patients (Solomon & DuMouchel, 2006).

Compared with absorption-based X-ray imaging techniques, phase-contrast imaging (PCI) techniques are much more effective in imaging low-density materials (Gao *et al.*, 1998; Lewis, 2004; Fitzgerald, 2000) and have been extensively studied for their promising prospects for biomedical imaging applications (Lewis *et al.*, 2005; Xi *et al.*, 2011; Stampanoni *et al.*, 2011). In the past several years, among the existing PCI techniques, grating interferometry has gained special attention for its soft tissue imaging capability (Pfeiffer *et al.*, 2007a;

Weitkamp *et al.*, 2008; Stampanoni *et al.*, 2011). In 2003, Momose *et al.* (2003) first demonstrated the feasibility of a two-grating interferometer in the hard X-ray regime with synchrotron radiation. Later, a three-grating interferometer was implemented with a tube-based X-ray source (Pfeiffer *et al.*, 2006) which opens up the possibility for its application in laboratory-based X-ray imaging systems. Subsequently, a reverse-projection tomographic method for a grating interferometer was developed which greatly reduces the exposure time (Zhu *et al.*, 2010). A two-dimensional X-ray grating interferometer has been realised to overcome the contrast lost in the direction parallel to the one-dimensional grating lines (Zanette *et al.*, 2010). Recently, the grating interferometer has been integrated into a compact cone-beam geometry gantry system (Tapfer *et al.*, 2011), which makes the technique much closer to clinical usage.

In the current study we report the development progress of a grating interferometer recently installed at the BL13W biomedical imaging beamline of SSRF and evaluate its performance by its imaging applications on biological specimens. The results are compared directly with those obtained from a conventional X-ray computed tomography system. The preliminary results confirmed the interferometer's efficiency in differentiating biological tissues with small density variations. In particular, we are successful in visualizing blood

vessels *in situ* in a formalin-fixed mouse without contrast agents.

2. Materials and methods

2.1. Set-up of the grating interferometer

At the BL13W beamline of SSRF, X-rays are emitted from a wiggler source with a wide energy spectrum (8–70 keV). The X-ray source has a size of 400 (H) $\mu\text{m} \times 24$ (V) μm and is located about 30 m away from the sample stage. The X-rays are monochromated using a double-crystal Si (111) monochromator ($\Delta E/E < 1.7 \times 10^{-3}$) and the corresponding beam size at the sample stage is about 40 (H) mm \times 3.5 (V) mm. In the current study the interferometer is scanned horizontally and its performance depends on the horizontal source size through the transverse coherence length l_c as defined by

$$l_c = \lambda D / \sigma_h, \quad (1)$$

in which λ is the X-ray wavelength, D is the source-to-sample distance and σ_h is the horizontal source size.

A schematic of the imaging set-up is shown in Fig. 1. It consists of a regular tomography stage, a phase grating (G1) and an absorption grating (G2) with their separated motorized stages. The gratings can move in both x and y directions in the plane orthogonal to the X-ray beam. They also have tilting stages which are useful in aligning the orientations of the grating lines. The gratings including their stages are mounted on an optical slide and the inter-distance between them can be adjusted either manually or by a motorized stage. In the current study the ordinary phase-stepping method is adopted to extract the phase information. It was implemented (Weitkamp *et al.*, 2005) by the movement of G1 with a 0.05 μm spatial resolution step motor along the transverse direction perpendicular to both the X-ray beam and the grating line directions. To cover the common X-ray energy range for biomedical applications, we designed three sets of G1 for 15, 20 and 33.2 keV X-ray energies which share the same G2. The gold height of G2 is about 50 μm . The period of G2 is 2.4 μm and the corresponding periods of G1 were designed taking into account the finite source-to-sample distance effect. The phase shifts of G1 were intentionally designed to be $\pi/2$, so the periods of G1 and G2 are about the same and the manufacturing of them can share the same mask using a novel LIGA process. In the set-up, projection images are captured by a CCD detector (Photonic Science, UK) with an effective pixel size of 9 μm and a field of view of 24 mm \times 36 mm which is placed right after G2.

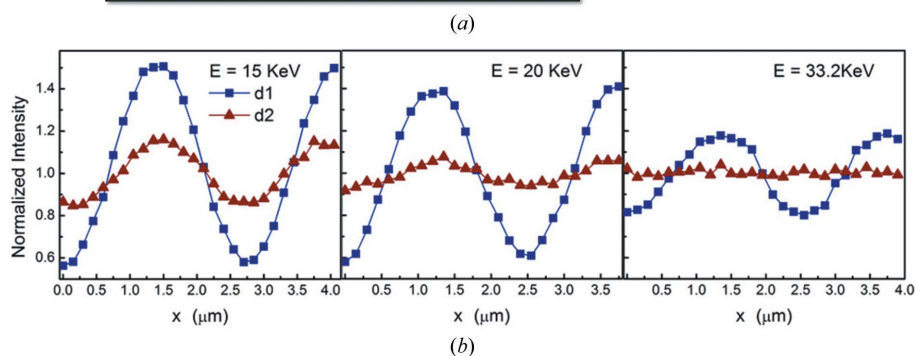
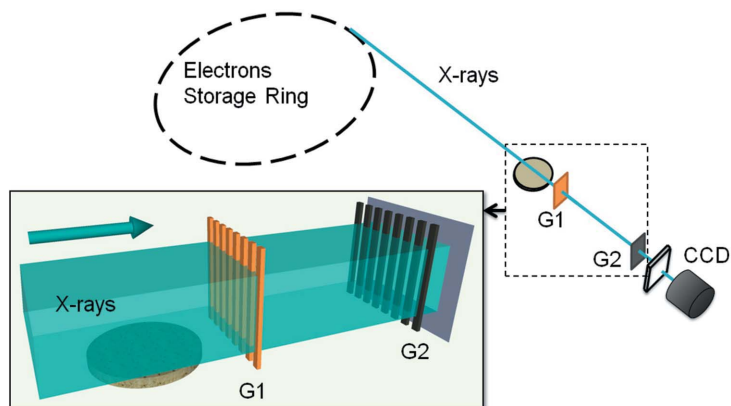


Figure 1

(a) Schematic of the X-ray grating interferometer set-up at the BL13W beamline of SSRF. (b) Plots of the intensity oscillations (normalized by mean intensity) as a function of the relative displacement x between the gratings for different X-ray energies using the corresponding grating sets.

2.2. Principle of the grating interferometer

The principle of the grating interferometry is based on the Talbot effect which has been elaborated in many previous studies (Weitkamp *et al.*, 2005; Momose *et al.*, 2003, 2006). Through the Talbot effect the phase modulation generated by the phase grating G1 is transformed into an intensity modulation downstream and analysed by the absorption grating G2, which is placed at a fractional Talbot distance d from G1,

$$d = Ng_2^2/2\lambda \quad (N = 1, 3, 5 \dots), \quad (2)$$

where g_2 is the period of G2.

When the phase-stepping method is employed, the intensity signal in each detector pixel will oscillate as a function of relative displacement x . The analysis of the intensity oscillations at each pixel with/without the sample can yield information about the absorption, phase change and scattering properties of the sample. Briefly, when the contributions from the high-order Fourier components are negligible, the intensity oscillation at each pixel can be approximated by only the zeroth and the first Fourier components as

$$I_x(x, y) = \sum_i a_i(x, y) \cos[(2\pi/g_2)x + \varphi_i] \simeq a_0(x, y) + a_1(x, y) \cos[(2\pi/g_2)x + \varphi_1], \quad (3)$$

where a_i is the amplitude coefficient and φ_1 is the phase shift. From (3), information including integrated attenuation coef-

Table 1

Parameters of the three sets of gratings designed for 15 keV, 20 keV and 33.2 keV, and their corresponding visibilities at different Talbot orders.

Energy (keV)	l_c (μm)	g_1 (μm)	g_2 (μm)	$d1$ (cm)	$d3$ (cm)	V_{d1}	V_{d3}
15	6.21	2.397	2.4	3.48	10.45	45.6%	15.6%
20	4.66	2.396	2.4	4.64	13.93	41.7%	8.02%
33.2	2.78	2.394	2.4	7.70	23.11	18.6%	~ 0

cient, phase shift and scattering can be retrieved and are expressed as

$$\mu = -\log(a_0/a_0^r), \quad (4)$$

$$\varphi = \varphi_1 - \varphi_1^r, \quad (5)$$

$$s = a_0^r a_1 / a_0 a_1^r, \quad (6)$$

where the superscript r denotes corresponding flat-field parameters with the object out of the X-ray beam. The phase shift of the intensity oscillation is proportional directly to the gradient of the integrated real part of the refractive index, δ , along the X-ray direction as

$$\varphi = \frac{2\pi d}{g_2} \frac{\partial}{\partial x} \left(\int \delta dz \right). \quad (7)$$

To yield high phase sensitivity, high-order fractional Talbot distances are preferred. However, owing to the finite transverse coherence length l_c , the intensity oscillation which is used in extracting the phase information will diminish considerably at high-order fractional Talbot distances. Visibility, which is the quantitative measure of this effect, is defined as

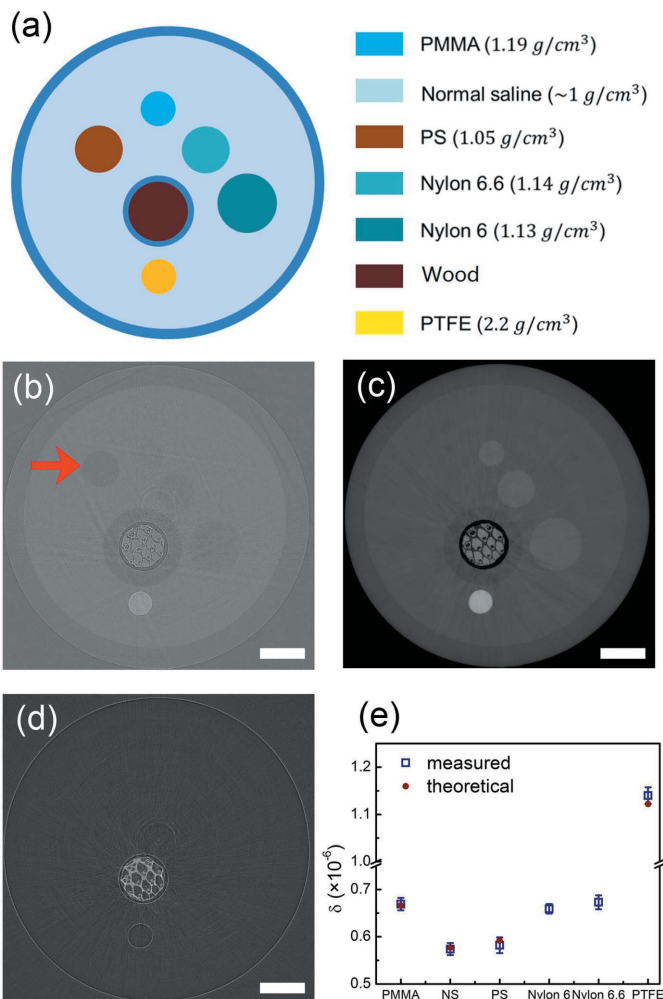
$$V = \frac{I_{\max} - I_{\min}}{I_{\max} + I_{\min}}, \quad (8)$$

where I_{\max} and I_{\min} are the maximum and minimum intensities in a pixel during a phase-stepping scan. In practice, a trade-off between sensitivity and visibility has to be reached. In our study we measured the intensity oscillation curves for all three sets of gratings at different Talbot distances and the results are plotted in Fig. 1(b). The corresponding visibilities are listed in Table 1. At 33.2 keV the visibility of the phase-stepping curve is almost zero at the third fractional Talbot distance.

By taking projection images around the sample, three-dimensional distributions of the attenuation coefficient, the refractive index and scattering properties of the sample can be reconstructed using an ordinary filtered-backprojection (FBP) algorithm or a modified FBP algorithm (Pfeiffer *et al.*, 2007b).

3. Phantom and biological specimens

A phantom consisting of several standard materials was utilized to investigate the phase sensitivity of the interferometer. The phantom is shown in Fig. 2(a), in which rods made of polymethylmethacrylate (PMMA), nylon 6.6, nylon 6, polytetrafluoroethylene (PTFE), polystyrene (PS) (all supplied by GoodFellow, Huntingdon, UK) and a toothpick


Figure 2

(a) Illustration of the phantom and the materials contained. Tomographic slices of the phantom, (b) the absorption coefficient tomogram, (c) the refractive index tomogram and (d) the scattering-based tomogram. (e) Reconstructed refractive indices of standard materials in the phantom together with theoretical values. Scale bar: 2 mm.

were placed in a micro-centrifuge tube filled with normal saline (NS). A tomography study of the phantom using the interferometer was carried out at 20 keV, in which 360 projection scans were carried out over 180°. Each phase-stepping scan consists of 16 steps to cover one full period of the intensity oscillation. The image exposure time is 15 ms. The total duration of one tomography study is around 120 min. The attenuation coefficient, the refractive index and scattering information can subsequently be obtained and the results are also shown in Fig. 2.

In our biomedical imaging application, two specimens were prepared. The first one was the right paw excised from a C57/Black6 mouse (weight 24 g) which was fixed in formalin solution over 24 h right after excision. The second one was the body of a new-born mouse (weight 5 g). The mouse was first anesthetized by using 50 mg kg⁻¹ ketamine and 10 mg kg⁻¹ xylazine intraperitoneally. Thoracotomy was then performed and a blunt needle was gently inserted into the left ventricle. The needle was connected with the outlet port of a three-way

valve, whose two inlet ports were in connection with a NS and a formalin container. NS (277 K) was perfused until the outflow from the right atrium was colourless. At the end of the NS perfusion the valve was switched to the formalin end to fix the vessel system. Finally, the full mouse body was fixed in formalin solution and only taken out during the imaging study. The whole procedure followed the standard laboratory animal use procedure approved by the Institutional Animal Care and Use Committee of the Shanghai Jiao Tong University.

To evaluate the difference in performance between the grating interferometer and a regular absorption-based set-up, the specimens were studied both by the grating interferometer and a MicroCT (Xradia, California, USA). The corresponding experimental parameters for both imaging modalities are summarized in Table 2.

4. Results and discussions

The reconstructed tomograms of the attenuation coefficient, the refractive index and the scattering property of the phantom are shown in Fig. 2. Comparing Fig. 2(b) with Fig. 2(c), it is obvious that the refractive index tomogram in general provides much better contrasts in distinguishing different materials in the phantom with the exception of the PS rod. The PS rod is almost invisible in the refractive index tomogram whereas it is still discernible in the attenuation one as indicated by the red arrow in Fig. 2(b). This anomaly is due to the fact that there exist no simple linear relationships between density, refraction index and attenuation coefficient. The PS rod has a 5% density difference from the surrounding NS solution, and about 50% difference in the attenuation coefficient, but only has less than 1.5% difference in the refraction index which is close to our detection limit. Fig. 2(d) shows the scattering-based tomogram in which the contrast from the non-uniform toothpick dominates over other uniform materials. This fact demonstrates the superiority of using the scattering information to study non-uniform materials.

Fig. 2(e) plots the reconstructed refractive indices of the materials in the phantom together with the theoretical ones obtained from the *XOP* software (del Rio & Dejus, 2004). The reconstructed refractive index and the corresponding standard deviation for each material were calculated from a selected uniform area in the tomogram. Despite the fact that the average refractive indices obtained agree nicely with the theoretical ones, the corresponding standard deviations are rather large. The imaging quality can be degraded by many factors including insufficient statistics, mechanical vibration, imperfect gratings and the unstable X-ray beam. In the current case we believe the major contribution of the error is the insufficient coherence and the strong-scattering wood. In Fig. 2(c) the conspicuous radial artefacts around the toothpick

Table 2

Experimental parameters for the tomographic scans of biological specimens.

	Grating interferometer		MicroCT	
	Mouse paw	Mouse body	Mouse paw	Mouse body
Rotation range (°)	0–180	0–180	0–360	0–360
Number of angles	360	720	1200	1200
Pixel size (µm)	9 × 9	9 × 9	9.6 × 9.6	10.5 × 10.5
Phase steps	16	16	–	–
X-ray energy	20 keV	20 keV	30 kVp	30 kVp
Projection exposure time	15 ms	16 ms	12 s	12 s
Total exposure time	86 s	184 s	4 h	4 h

after tomography reconstruction are clearly visible which induce large errors in the area of the uniform standard materials. Since ordinary biological samples are mainly composed of weakly scattering materials, the detection sensitivity of the current set-up can be higher as demonstrated in our subsequent studies on biological specimens.

For comparison, the biological specimens have been studied using both the grating interferometer and a regular MicroCT set-up. Fig. 3(a) shows the X-ray projection image of the mouse paw investigated. Tomograms obtained from both techniques at one cross section are shown in Figs. 3(b) and 3(c), respectively. Compared with the MicroCT, the grating interferometer shows exceptional imaging capability of soft tissues as showed by Fig. 3(c), in which clear tissue structures can be detected in the grating tomogram whereas they are totally absent in the MicroCT tomogram.

The comparison study on the new-born mouse has yielded similar results as the previous study. The grating interferometer demonstrated consistently better sensitivity in the detection of soft tissues than the MicroCT. For example,

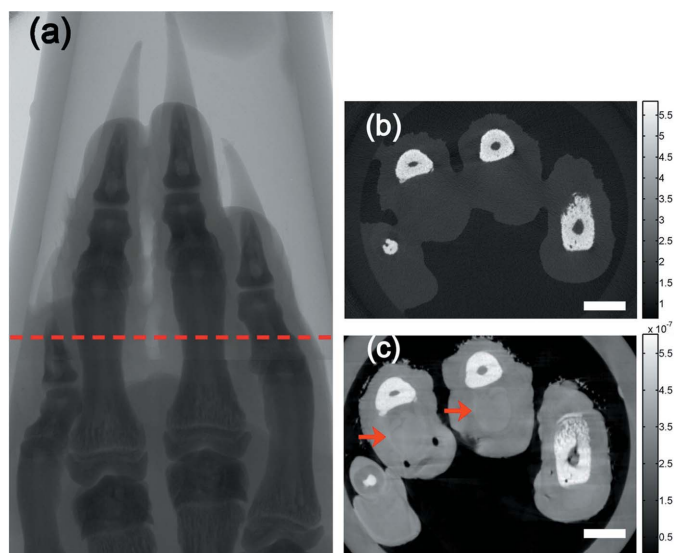


Figure 3

(a) X-ray projection image of a mouse paw. The dashed line indicates the reconstructed slices as shown in (b) [color bar: linear absorption coefficient (cm^{-1})] and (c) (color bar: refraction index δ) by the MicroCT and the grating interferometer, respectively. The red arrows in (c) show soft tissues which could be discriminated by the grating interferometer and are absent in (b). Scale bar: 1 mm.

tomograms obtained at one particular cross section close to the mouse chest by both techniques are shown in Figs. 4(b) and 4(c). Fig. 4(b) is almost featureless outside the bone area

whereas lots of structures are present in Fig. 4(c). We zoom in on the same parts of Figs. 4(b) and 4(c) and show them in Figs. 4(d) and 4(f). Fig. 4(d) is essentially a noisy background while Fig. 4(f) can reveal the fine structures in muscular tissues.

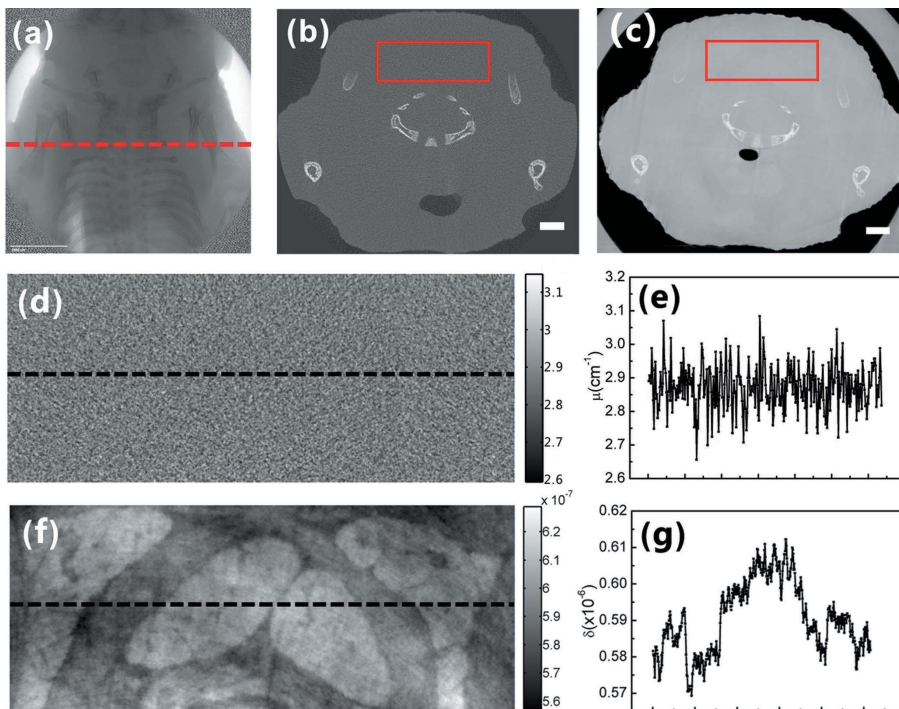


Figure 4

(a) X-ray projection image of a mouse body. The dashed line indicates the reconstructed slices as shown in (b) and (c) by the MicroCT and the grating interferometer, respectively. (d) [color bar: linear absorption coefficient (cm^{-1})] Enlarged view of the red box in (b); the linear absorption coefficient on the dashed line in (d) is plotted in (e), which shows no significant structure. (f) (color bar: refractive index δ) Enlarged view of the red box in (c), which is the same area shown in (d). (g) δ values on the dashed line in (f). Lots of structures can be seen in (f). Scale bar: 1 mm.

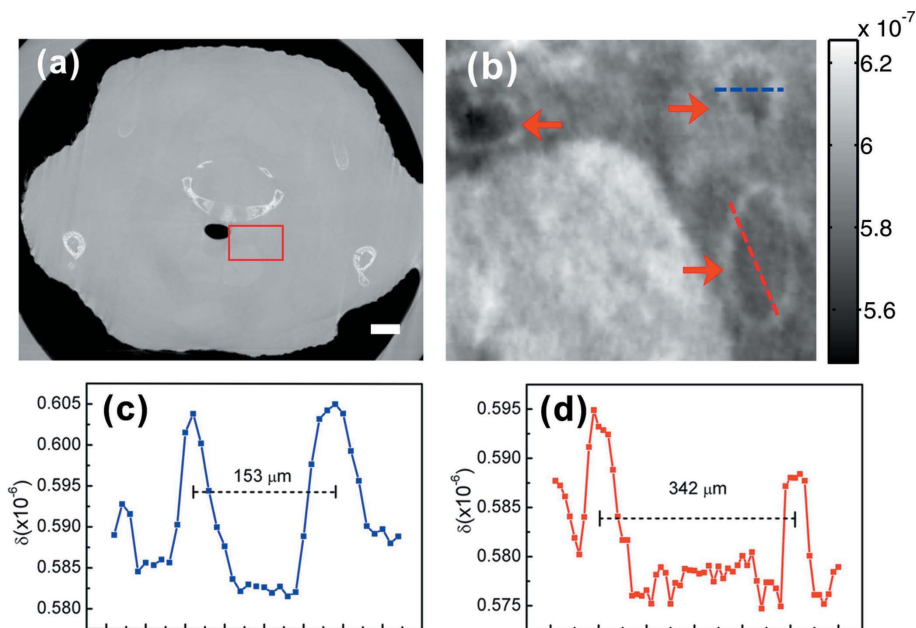


Figure 5

(a) Same cross section by the grating interferometer as in Fig. 4(c). (b) (color bar: refractive index δ) Enlarged view of the red box in (a), which reveals the presence of three blood vessels. The δ values along the blue and the red dashed lines across the blood vessels in (b) are plotted in (c) and (d). They are the carotid artery and carotid vein, respectively. Scale bar: 1 mm.

Most importantly, several circular structures stand out in the grating interferometer image, which is shown in Fig. 5(b). It turns out that the circular structures are blood vessel walls. Judging from their anatomical orientations and positions in three-dimensional space, the blood vessel that the blue dashed line goes across is the carotid artery, and the other one is the carotid vein. Since the blood vessels are filled with formalin, for the first time we can image *in situ* blood vessels inside a mouse without contrast agents. This implies great promise for its future biomedical imaging applications, especially for tumour angiography. The refractive index profiles along the dashed lines across the vessels are plotted in Figs. 5(c) and 5(d). It is evident that the interferometer can detect the refractive index change on the 5×10^{-9} level at 20 keV.

It is also important to compare the dosage in both comparison studies. It is worth noting that the single projection image dosage in the grating interferometer study is 0.9 mSv, similar to that in the MicroCT study. However, the phase-stepping technique requires 16 images at each projection angle, which significantly increases the dose delivered to the sample as compared with the MicroCT study. As a result, the accumulated dose is 5×10^3 mSv in the mouse paw experiment, and 1.5×10^4 mSv in the new-born mouse chest experiment for the grating interferometer study. This is to be compared with the several hundreds of mSv in the MicroCT study. Therefore, significant efforts are needed to improve over the traditional phase-stepping technique in reducing the dosage for the grating interferometer.

5. Conclusion

In conclusion, a grating interferometer designed for biomedical imaging applications was installed at SSRF. By conducting preliminary experiments on phantom and biological samples, the grating interferometer has shown good accuracy in quantitative phase imaging in addition to its excellent soft tissue imaging capability. In the biological experiments the carotid artery and carotid vein in a formalin-fixed mouse can be visualized *in situ* which suggests its broad prospects for tumour angiogenesis study. The performance of the grating interferometer can be further improved by both hardware and software upgrades.

This work was performed at the BL13W beamline of the Shanghai Synchrotron Radiation Facility and supported by the National Basic Research Program of China (973 Program; 2010CB834301), Shanghai Pujiang Program (10PJ1405600), Program for New Century Excellent Talents (NCET) in University and the Chinese National Science Foundation No. 11175121 and No. 11005074.

References

- Fitzgerald, R. (2000). *Phys. Today*, **53**, 23–26.
- Gao, D., Pogany, A., Stevenson, A. W. & Wilkins, S. W. (1998). *Radiographics*, **18**, 1257–1267.
- Hanahan, D. & Weinberg, R. A. (2000). *Cell*, **100**, 57–70.
- Lewis, R. A. (2004). *Phys. Med. Biol.* **49**, 3573–3583.
- Lewis, R. A., Yagi, N., Kitchen, M. J., Morgan, M. J., Paganin, D., Siu, K. K., Pavlov, K., Williams, I., Uesugi, K., Wallace, M. J., Hall, C. J., Whitley, J. & Hooper, S. B. (2005). *Phys. Med. Biol.* **50**, 5031–5040.
- Momose, A., Kawamoto, S., Koyama, I., Hamaishi, Y., Takai, K. & Suzuki, Y. (2003). *Jpn. J. Appl. Phys.* **42**, L866–L868.
- Momose, A., Yashiro, W., Takeda, Y., Suzuki, Y. & Hattori, T. (2006). *Jpn. J. Appl. Phys.* **45**, 5254–5262.
- Pfeiffer, F., Bunk, O., David, C., Bech, M., Le Duc, G., Bravin, A. & Cloetens, P. (2007a). *Phys. Med. Biol.* **52**, 6923–6930.
- Pfeiffer, F., Kottler, C., Bunk, O. & David, C. (2007b). *Phys. Rev. Lett.* **98**, 108105.
- Pfeiffer, F., Weitkamp, T., Bunk, O. & David, C. (2006). *Nat. Phys.* **2**, 258–261.
- Rio, M. S. del & Dejus, R. J. (2004). *Proc. SPIE*, **5536**, 171–174.
- Sekka, T., Volchikhina, S. A., Tanaka, A., Hasegawa, M., Tanaka, Y., Ohtani, Y., Tajima, T., Makuuchi, H., Tanaka, E., Iwata, Y., Sato, S., Hyodo, K., Ando, M., Umetani, K., Kubota, M., Tanioka, K. & Mori, H. (2000). *J. Synchrotron Rad.* **7**, 361–367.
- Solomon, R. & Dumouchel, W. (2006). *Invest. Radiol.* **41**, 651–660.
- Stampanoni, M., Wang, Z., Thüning, T., David, C., Roessl, E., Trippel, M., Kubik-Huch, R. A., Singer, G., Hohl, M. K. & Hauser, N. (2011). *Invest. Radiol.* **46**, 801–806.
- Tapfer, A., Bech, M., Pauwels, B., Liu, X., Bruyndonckx, P., Sasov, A., Kenntner, J., Mohr, J., Walter, M., Schulz, J. & Pfeiffer, F. (2011). *Med. Phys.* **38**, 5910–5915.
- Weitkamp, T., David, C., Bunk, O., Bruder, J., Cloetens, P. & Pfeiffer, F. (2008). *Eur. J. Radiol.* **68**, S13–S17.
- Weitkamp, T., Diaz, A., David, C., Pfeiffer, F., Stampanoni, M., Cloetens, P. & Ziegler, E. (2005). *Opt. Express*, **13**, 6296–6304.
- Xi, Y., Tang, R., Wang, Y. & Zhao, J. (2011). *Appl. Phys. Lett.* **99**, 011101.
- Zanette, I., Weitkamp, T., Donath, T., Rutishauser, S. & David, C. (2010). *Phys. Rev. Lett.* **105**, 248102.
- Zhu, P., Zhang, K., Wang, Z., Liu, Y., Liu, X., Wu, Z., McDonald, S. A., Marone, F. & Stampanoni, M. (2010). *Proc. Natl Acad. Sci.* **107**, 13576–13581.